International Journal of Heat and Mass Transfer 52 (2009) 5624–5633

Contents lists available at ScienceDirect

International Journal of Heat and Mass Transfer

journal homepage: www.elsevier.com/locate/ijhmt

An investigation of the influence of natural convection on tin solidification using a quasi two-dimensional experimental benchmark

Xiaodong Wang, Yves Fautrelle *

EPM/SIMAP/CNRS, BP75, 38402, Saint Martin d'Hères, Cedex, France

A R T I C L E   I N F O

Article history:
Received 12 June 2008
Received in revised form 11 May 2009
Accepted 11 May 2009
Available online 14 August 2009

Keywords:
Solidification
Benchmark
Natural convection
Liquid metal
Buoyant flow

A B S T R A C T

A well validated, quasi two-dimensional, unsteady solidification experimental benchmark is proposed to study the critical role of thermally driven natural convection using commercial pure tin. The experiment consists of solidifying a parallelipedic sample from two vertical sidewalls using two heat exchangers in a rectangular cavity. The mean temperature gradient G_T, and the mean cooling rate C_R, are set to control the experimental process. An array of 50 thermocouples allows us to measure the instantaneous temperature field and its evolution. While in the liquid state, the isotherms exhibit a plausible convective heat flow and its intensity increases as the Rayleigh number increases. In the solidification process, a novel recalescence phenomenon is observed by tracing the solidifying front in a relatively slow cooling rate case. By setting different mean temperature gradients, different patterns of the natural convection and the temperature field evolutions are obtained. A discussion is also presented regarding the crystallography.

1. Introduction

Heat, mass and solute transport phenomena via natural convection during metal/alloy solidification not only influences the movement of the melt–solid interface, but also changes the heat distribution globally, and consequently affects the morphology of solid/liquid interface, micro/macro structure, micro/macro-segregation, and freckles [1–8], and in consequence, the mechanical properties. Since so many conditioning thermal parameters need to be controlled in three-dimensional experiment [9–11], a quasi two-dimensional Cartesian geometry experimental model are occupied extensively study interesting [12]. The rectangular enclosure is insulated except for one vertical surface where the latent heat extracted, and the role of associated convective flow on solidification process were studied experimentally [3–5] and numerically [6,13–16]. It should note that the convective flow in this one-sidewall heat release experimental set-up is not strong and can not extend to the whole domain sufficiently due to the wall effect. The present study improves to two-sidewall thermal conditioning, which overcome above limit, and achieve significant natural convection. The pure metal can be use to do fundamental experiments without considering solute transport for simplifying the model [4].

The main purpose of the present work is to carry out a well instrumented benchmark experiment, and then investigate the influence of the pure thermal convection on pure metal solidification by looking at: (1) heat transfer in the whole experiment process, particularly in the phase-change process; (2) the relationship between thermodynamics and hydrodynamics in a liquid state; and (3) the mechanism by which thermal convection and latent heat release act on solidification, and their role during solidification.

Our results serve two purposes. First, they provide experimental evidence for the numerical models. However, they also provide quantitative results to study solidification, mechanism, or research on practical applications such as convection free crystal growth, heat flow in die or continuous casting.

A new quasi two-dimensional solidification benchmark experiment is established in the EPM/SiMAP/CNRS laboratory in France. The novel features of this experiment are as follows: two individually-regulated heat exchangers were designed, allowing different cooling rates to be set, which readily obtain the expected thermally or thermo-solutal driven convection. The newly designed heat exchangers significantly diminish experimental bias due to their higher heat transfer efficiency. Some new techniques are commonly used, this employs an automatic regulation technique based on heat radiation to ensure the precise insulating boundary conditions throughout the whole experimental procedure, which is essential to achieve a precise instantaneous temperature field. Another feature of this quasi two-dimensional benchmark is that a reliable identical micro-segregation distribution was obtained in both the median and surface planes.

Since three-dimensional model has complexities in heat and flow field structures, thus it is not easy to provide benchmark data, and we have stressed out our model as "quasi two-dimensional

---

* Corresponding author. Tel.: +33 476 82 5205; fax: +33 476 82 5249.
E-mail address: Yves.Fautrelle@simap.grenoble-inp.fr (Y. Fautrelle).

0017-9310/$ - see front matter © 2009 Elsevier Ltd. All rights reserved.
doi:10.1016/j.ijheatmasstransfer.2009.05.030

model". In the conclusion part, we will discuss and summarize this Hele–Show like benchmark model the reasonability taken as quasi two-dimensional.

The experimental set-up and configuration are presented in Section 2, and Section 3 aims to investigate the heat transfer in the liquid state and solidification process. The crystal growth and grain structure are illustrated in Section 4 and finally, some concluding remarks and perspectives are introduced in Section 5.

2. Quasi-2D experimental methodology

2.1. The experiment set-up

The experiment device consists of five major parts. The schematic sketch of which is illustrated in Fig. 1, and more details can be referenced in [17]. Important features of this apparatus are as follows:

(1) The dimension of the parallelepiped sample is $L = 10$ cm length, $W = 1$ cm width and $H = 6$ cm height. Beforehand, the tin is melted with a high frequency induction heating technique, and is quickly quenched into a water-cooling copper crucible, to get a pre-sample, and then is installed into a thin ($W_c = 1$ mm) stainless steel crucible.

(2) Fifty thermocouples were fixed on one of the largest surfaces of the crucible by laser-welding; on the opposite surface, the other sixteen thermocouples are arranged in the relative positions in order to calibrate temperature measurement. The interval distance in either the horizontal or vertical direction is 1.0 cm (see Fig. 1). Temperature fields and the evolutions are recorded during the melting/solidifying process by this thermocouple array. The relative accuracy of the temperature measurement is ±0.1 K and, the response time of the thermocouples is 0.7 s, the recording time step was 1.0 s. The reproducibility of the temperature measurement has been confirmed by comparing the temperature measurements across several experiments with identical experimental conditions. The temperature differences between these experiments are less than 0.5 K.

(3) The newly designed heat exchangers yield novelty features: they have the same cross-sectional shape (1 cm × 6 cm) of the sample in the y-direction to ensure the heat flux release through them being more homogenous; the compact three-part structure, cooper–stainless steel–cooper, is designed in order to shorten the heat transfer time; and to overcome chemical corrosion between tin and copper, two metal-layers Cr, Ni are deposited on the narrow vertical surfaces of the heat exchangers. The arrangement with six thermocouples in each heat exchanger (Fig. 1), with a vertical distance of 20 mm and a horizontal distance of 15 mm, allows us to measure the heat flux. Notice that the undesirable fluctuation in heat flux measurement temperature is significantly dampened compared with the previous configuration [4,18].

(4) An enclosure Kirchhoff box assures thermal insulation of the largest surface of the crucible via the heat radiation compensative method. This procedure is realized by a PID regulating system, the details can be found in [17,19].

(5) The entire set-up is installed inside a vacuum chamber in order to limit heat transfer by air convection and protect the sample from oxidation; the degree of vacuum is of the order of 0.01 atm.

2.2. Experimental procedure

A series of experiments have been performed using the following steps:

- Step 1: 0.42 kg of commercial pure tin is enclosed in a quartz cylinder, and is inductively melted, surrounded by a water-cooling copper coil delivering high frequency current. The melt is then quenched into a parallelepiped copper crucible, and a pre-sample is obtained.
- Step 2: The pre-sample is heated by the two heat exchangers, and the temperature is ramped up at a rate of 0.02 K/s, to avoid large temperature differences in the sample. When the control temperature reached 413 K, it is held for 10 min. The temperature is then continuously increased to 533 K, and is then held at this temperature for 30 min.
- Step 3: After the holding stage, the mean temperature gradient is manipulated by increasing the left wall temperature linearly to $G_TL/2$, and simultaneously decreasing the right wall temperature to $G_TL/2$, here, the mean temperature gradient G_T stand for the difference of wall temperature between two heat exchangers (ΔT) over the length $L = 10$ cm.

The heating/cooling rate was ±0.03 K/s via the controlled temperature regime with thermocouples FR3 and FL3 undergoing PID regulation. When the temperature reach the desired value, it is

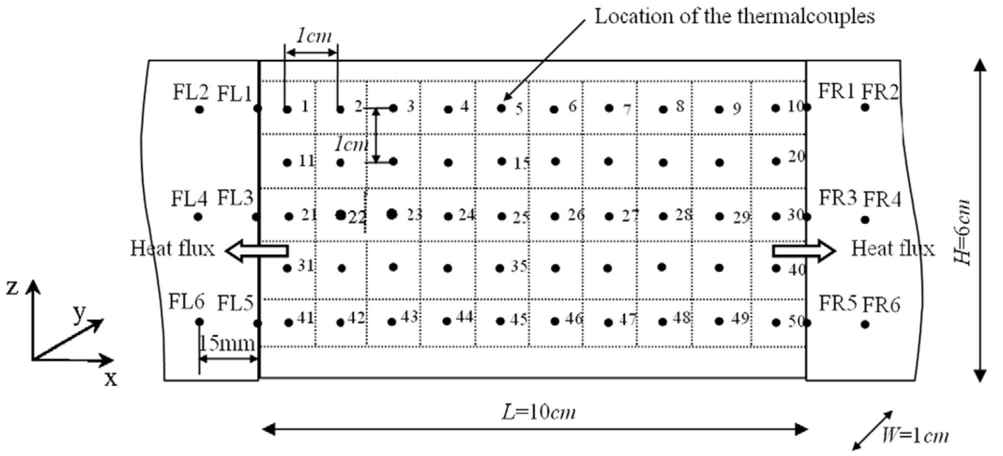

Fig. 1. Sketch of the solidification benchmark experiment, the location of the lateral thermocouples and the two heat exchangers.

then held for forty minutes to ensure the thermally driven convection extend well and is stabilized in the whole liquid domain.

- Step 4: The heat exchanger is set for cooling rates of 0.02, 0.03, and 0.04 K/s, respectively, and the temperature decayed until the solidification process is fully accomplished. The latent heat release and phase-change occurs in this step.

3. Heat transfer results

3.1. Symmetrical regime $G_T = 0$ K/m

A mean temperature gradient of $G_T = 0$ K/m indicates that the experimental control regimes (by FL3 and FR3) are the same on the both vertical sides (Fig. 1). The temperature profiles with the thermocouples TC25, TC26, …, TC30 (Fig. 1), and the corresponding heat powers passing by the two heat exchangers during the whole experimental procedure, are illustrated in Fig. 2. The heating rate is 0.02 K/s and, the cooling rate is 0.03 K/s.

A novel pseudo-plateau at the melting point $T_m = 504.97$ K appears in the fusion and freezing processes in Fig. 2(a). A huge latent heat release is observed, as shown in Fig. 2(b).

According to Fourier's heat law, the area integrations under the heat power curve over 4720–6070 s for the melting process, and 9100–10,200 s for the solidification process are computed, $P_e = 27.77$ kJ and the calorific capacity is $P_c = -3.98$ kJ. Thus, the experimental value of latent heat is $P_e + P_c = 23.79$ kJ. Furthermore, in the solidification process, $P_e = 20.43$ kJ, $P_c = 3.84$ kJ, $P_e + P_c = 24.27$ kJ, it is noticeable, that both heat variations are approximately equal to the theoretical latent heat value $L_f(\rho_S + \rho_L)V/2 = 24.29$ kJ.

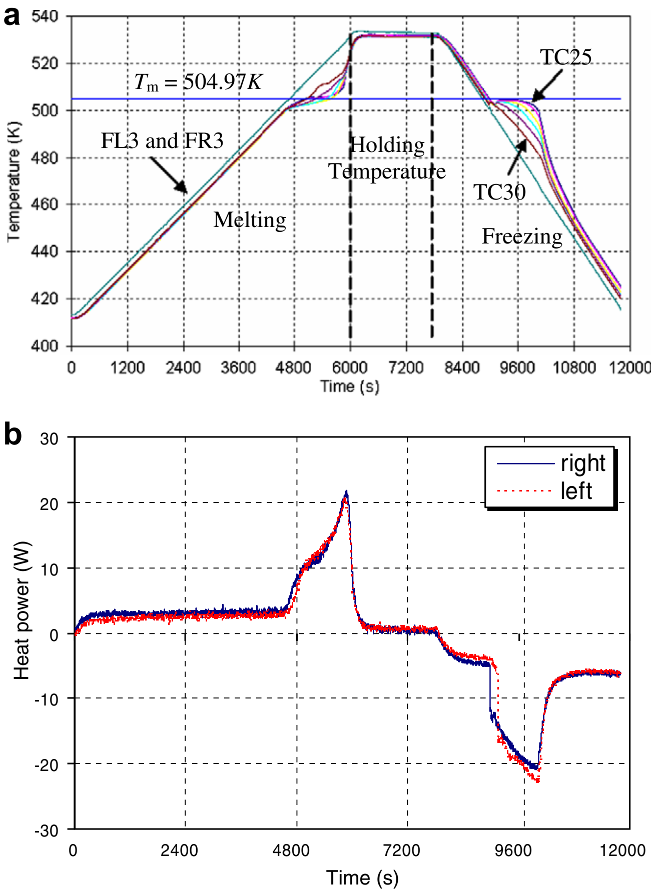

Fig. 2. Temperature profiles in the mid-height (see Fig. 1). (a) Heat power is released by the two heat exchangers. (b) When $G_T = 0$ K/m, the heating and cooling rates are 0.02 K/s and 0.03 K/s, respectively.

3.2. Unsymmetrical case: $G_T = 200$ K/m and $G_T = 400$ K/m

The temperature profiles and the heat power curves under the condition of $G_T = 200$ K/m and $C_R = 0.03$ K/s are shown in Fig. 3. The typical melting point pseudo-plateau is also observed in Fig. 3(a). Several heat varying processes can be readily identified in Fig. 3(b): 9000–9400 s is the holding liquid state, 9400–10,560 s is in the liquid cooling stage, and the phase-change is reached during 10,560–12,500 s. The temperature profiles and the heat power curves under the condition of $G_T = 400$ K/m and $C_R = 0.03$ K/s are shown in Fig. 4, it can be found that as the mean temperature gradient increases, the slope of the curvature around the melting point (Fig. 4(a)) is larger than that in Fig. 3(a), it may interpret that high intensity of the natural convection increases heat and mass transfer globally. As the heat flux shows in Fig. 4(a) and (b), 6600–7050 s is the holding liquid state, 7050–7600 s is in the liquid cooling stage, and the phase-change is reached during 7600–9600 s.

3.3. Thermal convection in the liquid state

In the temperature holding stage, the liquid metal is imposed by a certain mean temperature gradients, and the natural convection is generated, which is a typical Boussinq problem. The thermal flow goes upward in the vicinity of the hotter wall (left) and downward near the cooler wall (right) thanks to the variation in the density. Thus, a global thermally convective vortex is formed.

The temperature values distribute along the horizontal direction in the middle-height with thermocouples FL4, FL3, TC21,

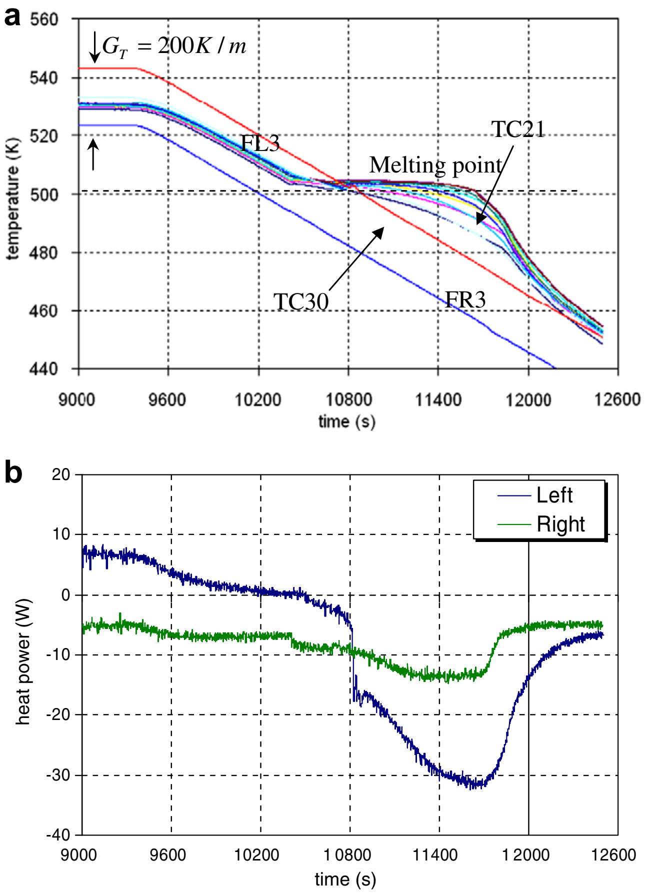

Fig. 3. Temperature profiles in the mid-height (see Fig. 1). (a) Heat power is released by the two heat exchangers. (b) When $G_T = 200$ K/m, $C_R = 0.03$ K/s.

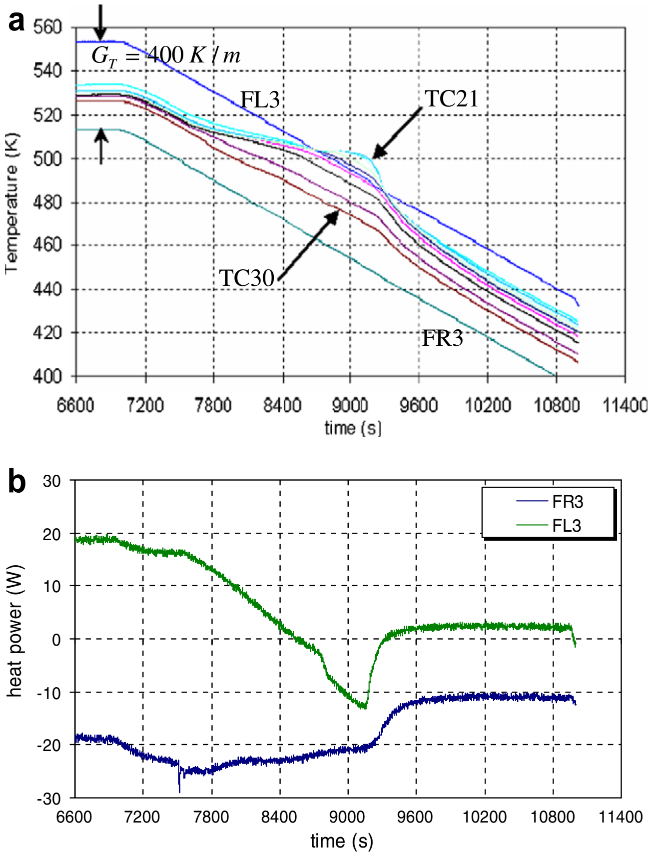

Fig. 4. Temperature profiles in the mid-height (see Fig. 1). (a) Heat power is released by the two heat exchangers. (b) When G_T = 400 K/m, C_R = 0.03 K/s.

TC22,. . ., TC29, TC30, FR3 and FR4 (see Fig. 1) for the various mean temperature gradients: G_T = 0, 100 K/m, 200 K/m, and 400 K/m are given in Fig. 4. In order to get the boundary temperature of the melt, heat flux conservation is applied to the cross-section of the heat exchangers and the melt near the sidewalls:

$$\lambda_{\mathrm{Cu}}(T_{\mathrm{FL4(or\ FR4)}} - T_{\mathrm{FL3(or\ FR3)}})/e_1 = \lambda_{\mathrm{Sn}}(T - T_{\mathrm{TC21}})/e_2. \tag{1}$$

where λ_{Cu}, λ_{Sn} are the conductivities of copper and tin, e_1 = 15 mm is the horizontal distance of the thermocouples, e_2 = 5 mm the distance between the vertical wall and the thermocouple close to it. The computing values are drawn in Fig. 4.

The vertical boundary temperatures of the samples, are determined by Eq. (1), they are also used as the thermal boundary conditions in the numerical simulation with the software package FLUENT. In order to have a precise comparison with the experiment, a three-dimensional model is adopted.

The experiment and the computing temperature profiles are plotted in Fig. 5. The interface temperature on the sample is calculated by Eq. (1), which is used as the boundary temperature for simulating study. Notice that a slight difference between experiment and computing result in case of G_T = 400 K/m, this might be explained by the fact that the temperature difference between the experiment and the simulation in case of 400 K/s may come from the heat lost increasing cause of radiation with the Kirchhoff box. The other cases of the computed and the experimental values are in approximate agreement with each other. Moreover, Temperature is found to be distributed linearly within the thermal boundary layer, whose thickness is $\delta_T \approx 6$ mm; thus the temperature values are measured by TC21/TC30 were located within the thermal boundary layers.

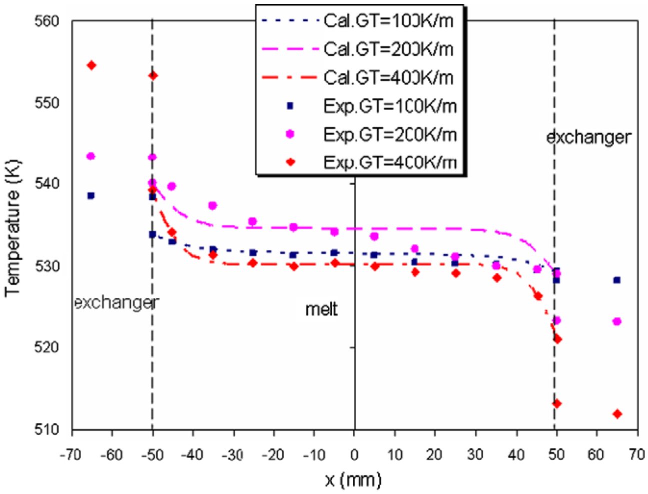

Fig. 5. Temperature variations in the horizontal at mid-height for various static mean temperature gradients in the liquid state of pure tin.

Similarly, we study the thermal flow boundary layers driven by natural convection with a method of fluid developing along vertical plane with a certain temperature difference [20]. Pure tin has a low-Prandtl number Pr = ν/a = 0.015 (ν, α are the kinematic viscosity and the heat diffusion of tin, respectively), which has a large inertial effect. The vertical Grashof number, Gr_H is,

$$Gr_H = \frac{g\beta\Delta T H^3}{\nu^2} = \frac{g\beta H^3}{2\nu^2 L}G_T \quad \text{or} \quad Ra_H = Gr_H \mathrm{Pr}, \tag{2}$$

where g is gravity acceleration, β is the expansion coefficient, ν is kinematic viscosity, and ΔT is the horizontal temperature difference between the two vertical sidewalls within the sample, which is estimated above. It indicates that Gr_H is proportional to the mean temperature gradient, G_T. The present case, $Ra_H < 10^9$, exhibits that the flow regime is laminar. Fig. 6 shows the isothermal contours and the local temperature gradients for three Ra_H. As Ra_H increases, the curvature of the isotherm becomes large and the intensity of fluid flow increases as illustrated in Fig. 6(a)–(c). It is seen in Fig. 6(c), where $Ra_H = 8.8 \times 10^5$, that the isotherm in the center part becomes an almost horizontal line; clearly, this indicates that the intensity of the buoyant flow becomes increasingly stronger. On the other hand, we can estimate the order of the typical velocity [4]:

$$U = \left(4g\frac{\Delta\rho}{\rho}H\right)^{1/2}, \quad \text{with} \quad \frac{\Delta\rho}{\rho} = \beta_T \Delta T = \frac{\beta_T \cdot G_T \cdot L}{2}, \tag{3}$$

where $\beta_T = 6.6 \times 10^{-5}\,\mathrm{K}^{-1}$, if ΔT = 40 K is selected, we have $U_0 \approx 4$ cm/s. The thickness of the flow boundary layer can be calculated by [20]:

$$\delta_v = \left(\frac{4\nu y}{U_0}\right)^{1/2} = y\left(\frac{Gr_y}{4}\right)^{-1/4} < \delta_T, \tag{4}$$

where δ_v is the flow boundary layer. This type configuration consists of fluid flow developing along the ambient walls and, creates conductive, convective heat transfer. It is appropriate to use adimensional Nusselt numbers to characterize heat and flow intensity, and thus, the local transfer coefficient h and Nusselt number Nu_y [20] are as follows:

$$h = -\frac{\lambda}{y}\left(\frac{Gr_y}{4}\right)^{\frac{1}{4}} \cdot \left.\frac{\partial T}{\partial x}\right|_{x=0} = \frac{\varphi}{y}\left(\frac{Gr_y}{4}\right)^{\frac{1}{4}}, \quad Nu_y \equiv \frac{hy}{\lambda}, \tag{5}$$

where $Gr_y = \frac{g\beta\Delta T y^3}{\nu^2}$. If we integrate along the vertical narrow surface, we can obtain the global mean Nusselt number, $\overline{Nu}$, developing along the height H:

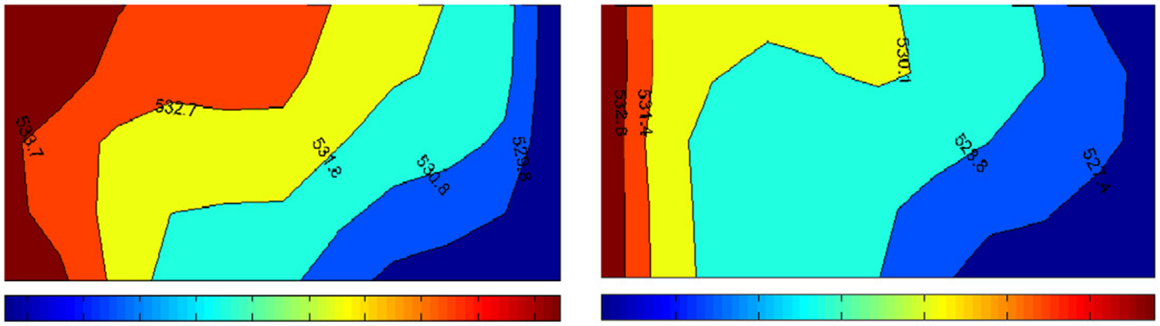

(a) $Ra_H = 2.2 \times 10^5$ (b) $Ra_H = 5.4 \times 10^5$

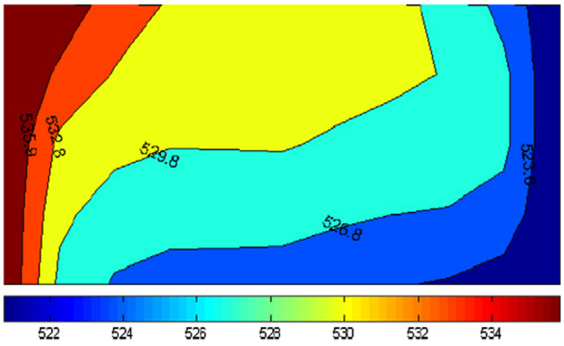

(c) $Ra_H = 8.8 \times 10^5$

Fig. 6. Thermal convection in the liquid state. Left: temperature contour; right: temperature gradient and isotherm. The represented scope is 10 cm × 4 cm (measurement zone: 9 cm × 4 cm) (see Fig. 1).

$$\overline{Nu} \equiv \frac{\bar{h}H}{\lambda}, \quad \text{and} \quad \bar{h} = \frac{1}{H}\int_0^H h dy = \frac{4}{3}\varphi\left(\frac{g\beta_T \Delta T}{4\nu^2 H}\right)^{\frac{1}{4}}, \tag{6}$$

where $\beta_T = 6.6 \times 10^{-5}\ \mathrm{K}^{-1}$, $\lambda = 30\ \mathrm{Wm}^{-1}\ \mathrm{K}^{-1}$, and $\nu = 2.86 \times 10^{-7}\ \mathrm{m\ s}^{-2}$. Finally,

$$\overline{Nu} \equiv \frac{4}{3}\left(\frac{g\beta_T H^3 \Delta T}{4\lambda \nu^2}\right)^{\frac{1}{4}}\varphi. \tag{7}$$

According to the above derivation, for the various cases of the mean temperature gradients in Fig. 6, we obtain $\overline{Nu} \equiv 100$ for $G_T = 100$ K/m; $\overline{Nu} \equiv 315$ for $G_T = 200$ K/m, and $\overline{Nu} \equiv 640$ for $G_T = 400$ K/m.

3.4. Phase-change evolution

The melting temperature isotherm can be followed and gives the shape of the solidification front. Two experiments with different mean cooling rates, $C_R = 0.02$ K/s, $C_R = 0.03$ K/s, and the same temperature gradient, $G_T = 0$ K/m, are examined.

The phase-change evolution is illustrated at nine selected time points in Fig. 7 for $C_R = 0.02$ K/s, and $G_T = 0$ K/m, and the experiment time is noted on each subfigure. Due to the influence of thermal convection, the starting solidifying position appears at the two bottom corners, and then the solidifying front proceed and produce a bowl-like shape as seen at $t = 9380$ s, and $t = 9410$ s. These may have resulted from two counter vortices going downward along the two vertical walls and upward in the center. Then, during the period 9410–9440 s, the solidifying front goes back towards the sidewalls. At about 9440 s, it became totally liquid, that is, the remelt phenomenon or the so-called recalescence occurs. A certain amount of latent heat is released from the melt, thanks to the phase-change, and it does not have enough time to be extracted by the heat exchangers. The period of heat release lasts about 30 s. The solidification restarts, and as the latent heat is near exhaustion, the natural convection becomes weak. The solidifying front curves become approximately parallel and vertical during the period 9540–12,000 s and then the liquid core becomes increasingly smaller. The liquid core has a spindle-like shape, and then disappears at the internal part of the domain, at about $t = 1290$ s. The last solidifying position is located in the upper-middle portion of the sample due to the difference in density between solids and liquids; thus, it is easy for shrinkage to occur at that position. It should be mentioned that the time of phase-change after remelt is significantly longer than that of the previous two stages, while the latent heat release plays the dominant role other than the natural convection during that period.

A phase-change evolution with a relatively high cooling rate, and $C_R = 0.03$ K/s, is exhibited in Fig. 8. Due to the more rapid cooling rate, the ratio of heat release is so high that the recalescence phenomenon is not observed. A similar shape for the solidifying front is found, but the last solidifying position is located in the upper portion. The whole solidification process is accomplished in about two minutes. Obviously, the effect of heat flow driven by natural convection is stronger than that of the previous case.

After comparing these cases, it is evident that the lower cooling rate easily forms recalescence phenomena.

3.5. Temperature field evolution

Obtaining the available temperature field and its evolution is one of the fundamental objectives of a solidification benchmark experiment. Two cases with different mean temperature gradients are introduced in the following sections.

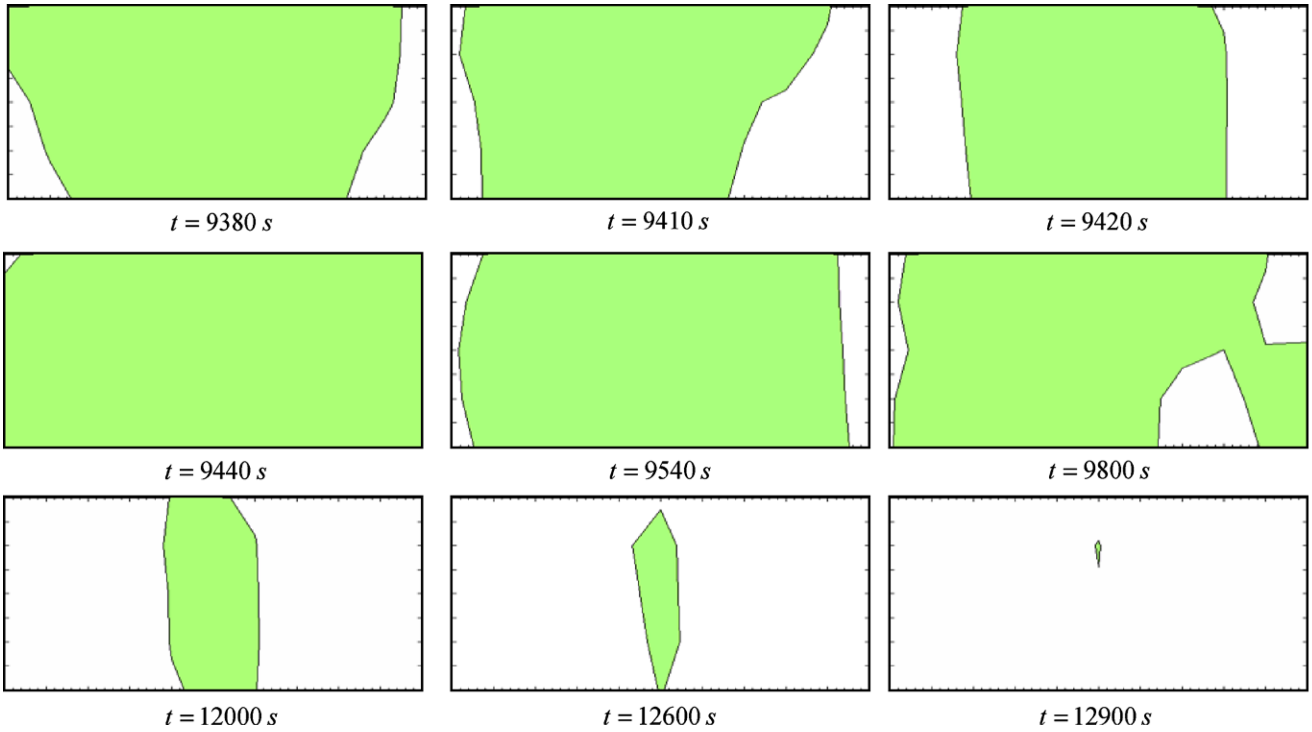
$t = 9380\,s$ $t = 9410\,s$ $t = 9420\,s$

$t = 9440\,s$ $t = 9540\,s$ $t = 9800\,s$

$t = 12000\,s$ $t = 12600\,s$ $t = 12900\,s$

Fig. 7. Phase-change evolution or the observation of recalescence phenomena produced by tracing the solidifying front trace. $G_T = 0$ K/m, $C_R = 0.02$ K/s (measurement zone: 9 cm × 4 cm).

3.5.1. Symmetrical case: $G_T = 0$ K/m

Temperature field evolution is shown in Fig. 8 at four representative time points with the conditions $G_T = 0$ K/m, $C_R = 0.03$ K/s. The temperature map at $t = 5350$ s (Fig. 9a) illustrates the situation near the end of the melting process, the last melting zone, yielding a melting point temperature of 504.97 K, largely distributed in the center. The boundary layer accumulates the majority of temperature variation. Fig. 9(b) exhibits the heat flow in the total liquid state at $t = 8600$ s. The flow pattern suggests that two counter vortices of heat flow act in the liquid metal. This flow pattern could not be observed in the associated numerical study, it might result from assumption of thermal diffusion will be very quickly accomplished in liquid state, thus the temperature difference within the liquid cannot build, while this temperature different is necessary to generate convective flow. Fig. 9(c) shows the temperature map, in which the last solidifying zone remains in the upper-center part, although the natural convection at this moment becomes very weak since the solidification is near the end. However, the flow pattern changes a little compared to Fig. 9(b). Fig. 9(d) shows the situation after the phase-change process has been finished; the temperature is inversely distributed as shown in Fig. 9(a).

3.5.2. $G_T = 400$ K/m

Fig. 10 shows temperature field evolution during solidification under the conditions $G_T = 400$ K/m, $C_R = 0.03$ K/s. Fig. 10(a) shows the moment ($t = 7600$ s) the solidification begins from the bottom-right corner; the tendency of natural convection is indicated by the dark line and the arrows. The isotherm of the melt point temperature extends from the right to the left. Moreover, Fig. 10(b) exhibits the liquid–solid coexist state; the temperature

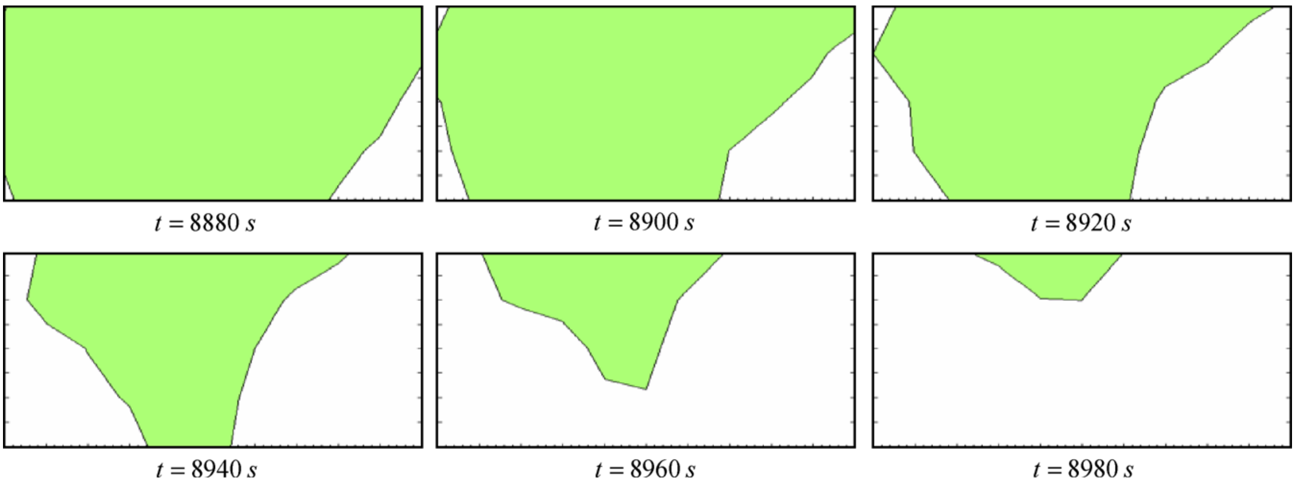
$t = 8880\,s$ $t = 8900\,s$ $t = 8920\,s$

$t = 8940\,s$ $t = 8960\,s$ $t = 8980\,s$

Fig. 8. Phase-change evolution. $G_T = 0$ K/m, $C_R = 0.03$ K/s (measurement zone: 9 cm × 4 cm).

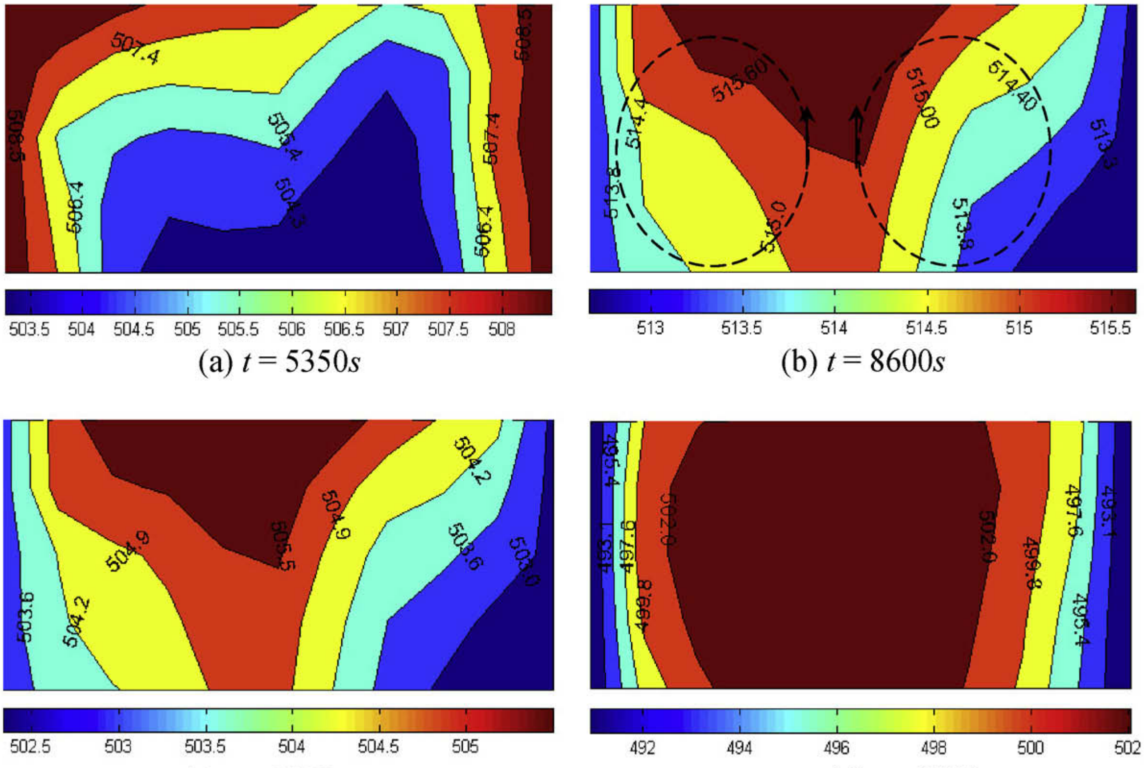

(a) $t = 5350s$ (b) $t = 8600s$

(c) $t = 8950s$ (d) $t = 9500s$

Fig. 9. Temperature evolutions during the melting and freezing processes. $G_T = 0$ K/m, $C_R = 0.03$ K/s.

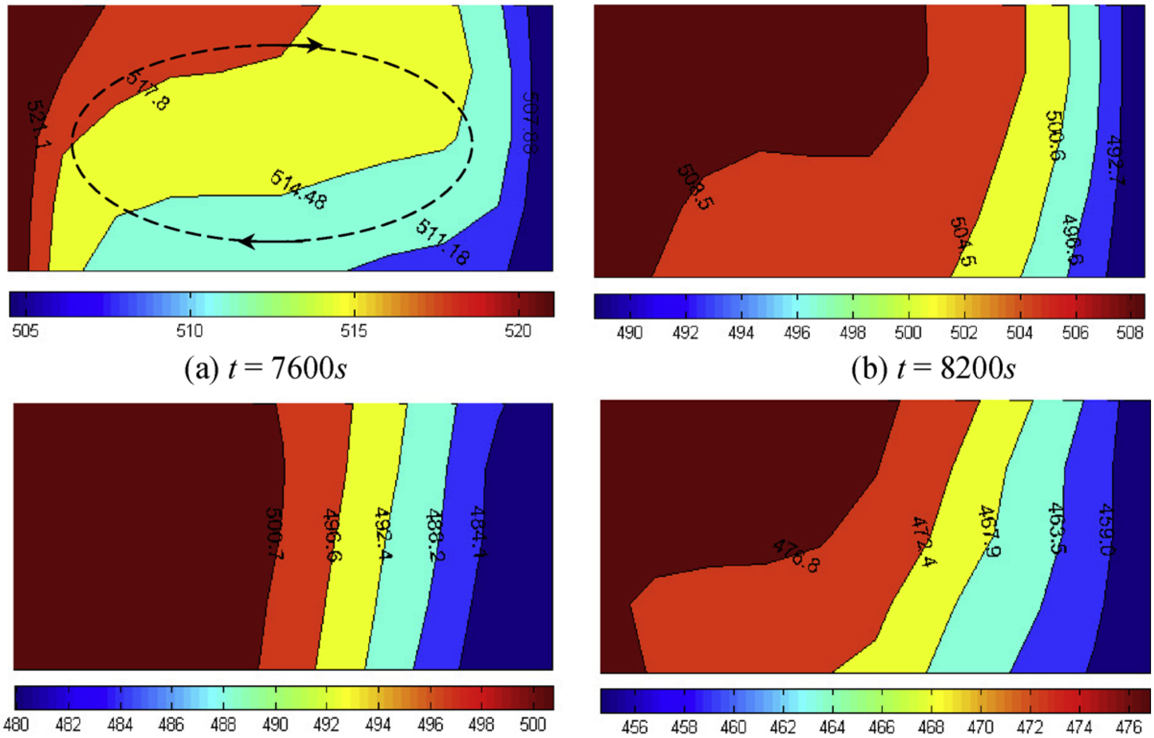

(a) $t = 7600s$ (b) $t = 8200s$

(c) $t = 8800s$ (d) $t = 9400s$

Fig. 10. Temperature field evolution during solidification. $G_T = 400$ K/m, $C_R = 0.03$ K/s.

contour curvature in the liquid zone follows the trend of the thermally convective flow. In Fig. 10(c) at $t = 8800$ s, the temperature decays under the melt point temperature, but due to the latent heat, it is not entirely exhausted; the distribution of isotherms is still inhomogeneous. This inhomogeneous temperature zone finally disappears at about $t = 9200$ s, as illustrated in Fig. 10(d).

4. Crystal growth

Macroetching methods are used to reveal the macrostructure of the sample. Acid (75 vol.% HCl + 25 vol.% HNO_3) is used to treat the samples in their largest median planes. A comparative metallographic study has been performed for various mean temperature gradients $G_T = 100$ K/m, $G_T = 200$ K/m, $G_T = 400$ K/m at $C_R = 0.03$ K/s, as shown in Fig. 11.

In this study, the grains are grown from the two vertical sidewalls. It is found that in cases of relatively low mean temperature gradients, as in Fig. 11(a) and (b), the columnar grains are coarse. The low growing orientation may be explained by the low local temperature gradients of the melt, and the slow interface growth velocities. Particularly in the case introduced in Section 3.4, it is possible to remelt, and the heat effect of latent heat release is higher than the effect of natural convection during the solidification process. Again, when the melt is solidified with high mean temperature gradients as shown in Fig. 11(c), the influence of natural convection is significant and the columnar grains grow against the thermal convective flow (Fig. 10(a)). Also, thanks to higher local temperature gradients and higher cooling rates, the columnar grains align closely and become fine. Another observation is that the cracks can be observed in Fig. 11(c), as indicated by an arrow. It is remarkable that the columnar grains crash at that location and the density difference is large thanks to the last solidification zone; therefore, we may conclude that huge stresses must exist at that point.

Generally speaking, the crystal growth of the pure metal is columnar, while we observed a few equiaxed grains in three samples. These may result from one of two sources: other chemical elements, which may improve equiaxed growth, that are included in the commercial pure tin; variation in the orientation of columnar growth; or inverse growth, which may cause competition between crystals, and then a collision caused by the influence of the natural convection, thus forming equiaxed grains.

5. Concluding remarks and perspectives

A quasi two-dimensional benchmark experimental model has been established. The influence of natural convection with pure tin on solidification has been examined in the present study. Furthermore, thermal convection has been confirmed by measuring the temperature field and its evolution.

The reasons of such experimental model being considered as a quasi two-dimensional benchmark are as follows:

(1) The geometry of the sample, the ratio length–width is $L/W = 10$, the height–width $W/H = 6$.
(2) Three-dimensional numerical study shows that in the thickness direction the quasi two-dimensional flow can extend to about 0.8 cm (for 1 cm width) from the median plane to the biggest walls.
(3) In Section 3.3, the theoretical analysis of the boundary thickness provides the flow boundary layer and thermal boundary layer basis, which valid these 3D effects (wall effect) can then be reasonable smaller.
(4) The macrostructures of the sample on the surface (taken at 1 mm to the biggest sidewalls) and in the median plane are almost the same, that is, the macrostructure in the different slices along the third-direction have almost the same distributions, this implicit that the heat transfer has little difference in the thickness direction during the solidification. While in the previous case that has a large difference [18]. Again, the heat transfer between the crucible and the

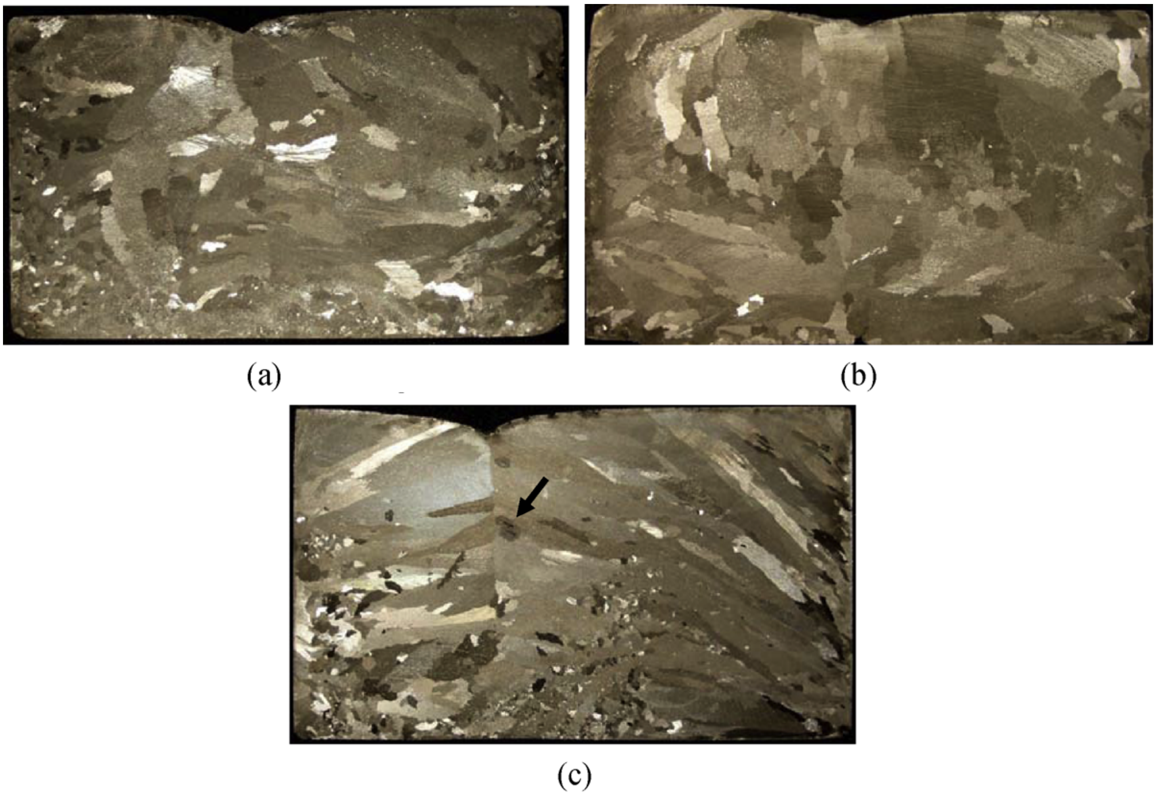

Fig. 11. Grain structure, $C_R = 0.03$ K/s. The mean temperature gradients are (a) $G_T = 100$ K/m; (b) $G_T = 200$ K/m; and (c) $G_T = 400$ K/m.

melt is ignorable small [19], the heat transfer via radiation can be omitted and the temperature difference across the thickness of the crucible and the melt are enough small [19].

(5) As discussion in Section 3.1, the heat loss is justified by integral the heat flux over the experiment time, which does not play the dominate role in the whole heat transfer process.

The intensity of natural convection increases as the mean temperature gradient increases. Thermal analysis, including thermal/hydrodynamic boundary layers, has been performed experimentally and quantitatively. Heat transfer and latent heat release during the phase-change are characterized through the heat flow patterns, and a particular recalescence phenomenon in slower cooling rate cases is confirmed by tracing the solidifying front.

The experimental set-up has proven its ability to obtain well-controlled solidification. Thus, based on the study of pure tin solidification, the influence of natural convection with the binary or ternary metallic alloy on solidification is also examined in this benchmark experiment where the solute-rejecting process can also be considered. The influence of natural convection on macro-segregation has raised another interesting topic.

It is well known that manipulation of various measures can significantly affect grain structures. For example, the mean temperature gradient and the mean cooling rate can be used to adjust the local temperature gradients, the melt–solid cooling rate, or the liquidus interface velocity. Our understanding of the mechanism of columnar-to-equiaxed grains transition can also be improved by the present benchmark study.

Magnetic fields and electromagnetic forces have also long been used to control the flow of a solidifying melt. The purposes for this include stirring the melt in order to remove inclusions, controlling the grain structure and size, and improving the homogeneity of temperature and composition. Moreover, the external force improves the defects of macro-segregation. Recently, a numerical simulation suggested that the melt flow in a mushy zone, generated by a periodically reversed driving force, might be particularly efficient to reduce the macro-segregation in the solidified material [21]. Thus, the influence of forced convection by normal or modulated electromagnetic forces can be examined in this benchmark.

Acknowledgments

The authors acknowledge the ESA (Europe Space Agent) through the CETSOL (Columnar-to-Equiaxed transition of SOLidification) project (ESA-MAP AO-99-117) for its financial support.

Appendix A. Thermo-physical properties of pure tin

From Table 1, we can see that the density variation can approximately in agreement with Boussinesq approximation. Table 1 lists some other thermo-physical properties of pure tin in our study range as well.

Table 1
The thermo-physical properties of pure tin [22,23].

	Definition	Temperature (K)	Values	Units
T_m	Melting point		504.928	K
ρ	Density	500	7179	kg/m^3
		505	7079	kg/m^3
		600	6911	kg/m^3
		700	6838	kg/m^3
C_p	Heat capacity	298	228	$J\,kg^{-1}\,K^{-1}$
		505	250	$J\,kg^{-1}\,K^{-1}$
		573	242	$J\,kg^{-1}\,K^{-1}$
λ	Thermal conductivity	373	63	$W\,m^{-1}\,K^{-1}$
		473	60	$W\,m^{-1}\,K^{-1}$
		505	30.0	$W\,m^{-1}\,K^{-1}$
		573	31.4	$W\,m^{-1}\,K^{-1}$
L_f	Latent heat of fusion		59.6	kJ/kg
ν	Kinematic viscosity		2.5×10^{-7}	$m^2\,s^{-1}$
α	Thermal diffusivity		1.86×10^{-5}	$m^2\,s^{-1}$

Appendix B

An integrated form of the global heat transfer equation is provided by Quillet and Fautrelle in a previous study [4], in which a quantity of an average temperature was introduced. However, thanks to the large individual difference of the temperature in the space domain and the limited numbers of thermocouples, particularly in the case of high mean temperature gradient, this method can only provide a rough estimation of the global heat transfer process. Alternatively, a derivative equation, addressing the heat flow process, is given:

$$P_e + P_c + P_l = \int_V \rho c_p \frac{\partial T(x,y,t)}{\partial t} dv + L\frac{dm_s}{\partial t}, \tag{A.1}$$

where ρ, L, m_s, c_p are the density, latent heat of fusion, the mass of the solid phase and the heat capacity, respectively; P_e, P_c, P_l on the LHS represent the heat powers passed by the two heat exchangers, the unavoidable heat capacity of the stainless steel crucible absorbing heat during fusion, and other heat lost, respectively. The first term on RHS is the heat capacity variation; the second term is latent heat release. With an adequate heat-insulating condition in the surrounding environment, P_c, P_l are negligibly small. By setting a linear temperature drop that occurs inside the heat exchangers rather than in the sample, it is possible to get well-controlled heat flux P_e) and observe the heat transfer evolution information. The two terms on RHS of Eq. (A.1) provide an example of this point.

References

[1] J.E. Drummond, S.A. Korpela, Natural convection in a shallow cavity, J. Fluid Mech. 182 (1987) 543–564.
[2] S. Asai, I. Muchi, Modelling of convection during solidification of metal and alloys, ISIJ. 18 (1978) 90–98.
[3] D.J. Hebditch, J.D. Hunt, Observation of ingot macrosegregation on model systems, Metall. Trans. 5 (1974) 1557–1564.
[4] G. Quillet, Y. Fautrelle, A benchmark solidification experiment on a Sn–10 wt% Bi alloy, Int. J. Heat Mass Transfer 50 (2006) 654–666.
[5] T. Tagawa, G. Authie, R. Moreau, Buoyant flow in long vertical enclosures in the presence of a strong horizontal magnetic field. Part 1. Fully-established flow, Eur. J. Mech. B 21 (2002) 383–398.
[6] Ch.J. Vives, Solidification of tin in the presence of electric and magnetic fields, Cryst. Growth 76 (1986) 170–184.
[7] O. Bertrand et al., Melting driven by natural convection – a comparison exercise: first results, Int. J.Therm. Sci. 38 (1999) 5–26.
[8] H. Yin, J. Koster, In situ observation of concentration stratification and solid–liquid interface morphology during Ga–5% In alloy melt, Cryst. Growth 205 (1999) 590.
[9] Y. Lu, C. Beckermann, A. Karma, Convection effects in three-dimensional dendritic growth, IMECE-ASME, New Orleans, Louisiana, November, 2002, pp. 1–6.
[10] N. Ramachandran, J.P. Gupta, Y. Jaluria, Experiments on solidification with natural convection in a rectangular enclosed region, Int. J. Heat Mass Transfer 4 (1982) 595–596.
[11] N. Ramachandran, J.P. Gupta, P.G. Daniels, The thermal and fluid effects during solidification in a rectangular enclosure, Math. Phys. Sci. 440 (1993) 273–289.
[12] P.G. Daniels, High Rayleigh number thermal convection in a shallow laterally heated cavity, Math. Phys. Sci. 8 (1993) 273–289.
[13] G. Guillemot, Ch.A. Gandin, M.J. Bellta, Interaction between single grain solidification and macrosegregation: application of a cellular automaton-finite element model, Cryst. Growth 303 (2007) 58–68.
[14] G. Shiralkar, A. Gadgil, C.L. Tien, A numerical study of laminar natural convection in shallow cavities, Int. J. Heat Mass Transfer 4 (1981) 1621–1629.
[15] V.R. Voller, C. Prakash, A fixed grid numerical modeling methodology for convection–diffusion mushy region phase-change problems, Int. J. Heat Mass Transfer 8 (1987) 1709–1719.
[16] A.K. Singh, R. Pardeshi, B. Basu, Modelling of convection during solidification of metal, Sadhana 26 (2001) 139–162.
[17] X.D. Wang, Y. Fautrelle, A quasi two-dimensional benchmark experiment for the solidification of a tin–lead binary alloy, C. R. Mécan. 335 (2007) 335–341.

[18] G. Quillet, Meso-segregation during solidification in a binary alloy under the influence of convection, Ph.D. Thesis, INPG Grenoble, France, 2003.
[19] X.D. Wang, Y. Fautrelle, Temperature field evolution in a horizontal solidification experiment and its influence on macrostructure, MCWASP XI, Opio France, May, 2006, pp. 391–398.
[20] A.M. Bianchi, Y. Fautrelle, J. Etay, Heat transfer, PPUR (2004) 149.
[21] X.D. Wang, A. Ciobanas, Y. Fautrelle, Control of the macro-segregation during solidification of a binary alloy by means of an AC magnetic field, Mater. Sci. Forum 508 (2006) 163–168.
[22] W.F. Gale, T.C. Totemeier (Eds.), Smithells Metals Reference Book, eighth ed., Elsevier Butterworth-Heinemann Ltd., Oxford, UK, 2004, pp. 1414–14-29.
[23] S.V. Stankus, R.A. Khairulin, The density of alloys of tin–lead system in the solid and liquid states, High Temp. 44 (2006) 389–395.